Compression performances and failure maps of sandwich cylinders with pyramidal truss cores obtained through geometric mapping and snap-fit method

Jiangtao Wang[a,b], Wenfeng Liu[a,b], Shuai Kang[a,b], Te Ma[a,b], Zhe Wang[a,b], Wu Yuan[a,b,*], Hongwei Song[a,b], Chenguang Huang[a,b]

[a] *Key Laboratory for Mechanics in Fluid-Solid Coupling Systems, Institute of Mechanics, Chinese Academy of Sciences, Beijing 100190, China*
[b] *School of Engineering Sciences, University of Chinese Academy of Sciences, Beijing 100049, China*

ARTICLE INFO

ABSTRACT

The compressive behaviors and failure maps of lightweight all-metallic sandwich cylinders with pyramidal truss cores are studied experimentally and theoretically. Orthotropic truss cores are fabricated through geometric mapping and snap-fit method. Curved facesheets are bonded to the truss cores by two-times vacuum brazing approach to eliminate unbound nodes. The full-field deformation and strain of the sandwich cylinder are measured by using the 3D digital image correlation system. The local buckling of the facesheet, the mode of which is influenced by the truss cores, is observed during the experiment. Theoretical models are developed considering five possible failure modes of the sandwich cylinder under compression, namely, Euler buckling, global buckling of the cylinder, local buckling of facesheet, face yielding and core member buckling. Failure maps are constructed on the basis of the models. The typical failure modes obtained from numerical simulation are consistent with the theoretical prediction.

1. Introduction

A sandwich structure with different topological truss cores is a type of lightweight structure with excellent load capacity and multi-functionality [1], and it has attracted the attention of many researchers. Over the past two decades, various lattice core configurations have been proposed including honeycomb grid [2], corrugated grid [3,4], pyramidal truss [5–7], Kagome lattice [8], and tetrahedral truss [9,10]. Several fabrication methods for core construction have been proposed including fused deposition modeling [11], perforated sheet folding/drawing [1], interlocking [12–14], and hot mold pressing [10]. Among these topologies, lattice truss with pyramidal cell topology is a typical static determinant, stretch-dominated structure [15], as the effective strength and equivalent Young's modulus are linear to its relative density. Meanwhile, open-cell core construction is convenient for free fluid flowing [16] or solid filling [17,18], thereby extending the usage of sandwich panels to multi-functional applications.

For the sandwich cylinder structure, which is limited by the difficulties in the design and manufacturing process, the core space is mainly filled with closed-cell 2D configurations [19–22] or metal foam

[23]. Study on sandwich cylinders with open-cell lattice cores are limited. Xiong et al. [24,25] proposed a hybrid sandwich cylinder with curved metallic quasi-pyramid lattice core and composite facesheets. The quasi-pyramid lattice core configuration is enhanced with straight rods to strengthen the connection with the facesheets, adding an extra core mass. Yang et al. [26] proposed a composite sandwich cylindrical shell with pyramidal truss-like cores. However, these proposed pyramidal core configurations are not isotropic along the normal direction inside and outside the surface. Thus, the truss core structure is inefficient.

Failure modes of the sandwich structure are controlled by the geometric parameters of facesheets and truss cores. Hence, the construction of mechanism maps is an effective means of predicting the failure mode. Agarwal et al. [27] presented optimum designs for unstiffened, hat-stringer-stiffened, and honeycomb sandwich cylinders under axial compression. They found that the honeycomb core configuration offers considerable weight savings. Hutchinson and He [23] studied the buckling response of cylindrical sandwich shells with foamed metal cores subject to axial compression. The interaction between the imperfections of shells and plastic yielding was examined. For sandwich

cylinders filled with different close-cell 2D configurations, theoretical analyses are based on the smearing method suggested by NASA [21]. For sandwich cylinders with open-cell lattice cores, the constraints of the truss cores to the facesheet are weaker than the closed-cell configurations mainly provided by nodal joints. Therefore, the failure modes of the sandwich cylinders, especially that of the facesheet are different. Experimental and analytical investigations are conducted to examine such failure modes.

To the best knowledge of the authors, no research work on sandwich cylinders with fully pyramidal truss cores made from one single material has been reported. In this paper, a universal fabrication method for sandwich cylinders with truss cores using an interlocking method is proposed. The axial compression behaviors of sandwich cylinders with pyramidal truss core are revealed by theoretical analysis and experimental investigations. Sandwich cylinders with pyramidal truss core integrated with a metallic material perform better than single-walled cylinders, and their applications in load bearing and thermal structures are unlimited.

2. Fabrication of sandwich cylinder with pyramidal truss core

2.1. Design method

The geometrical parameters of pyramidal truss core in the sandwich cylinder are designed on the basis of the topological configuration of that in the sandwich panel. The rectangular unit cell of the plane structure is mapped into an annulus cell, with the length of central line (l_c) and the core thickness (t_c) unchanged, as shown in Fig. 1. The angles between the truss members are changed from the original inclination angle between truss θ to different values, with θ_1 at the outside facesheet and θ_2 at the inside facesheet. The equivalent angle between the core member and radial axis $\bar{\theta}$ is defined as the average value of θ_1 and θ_2, that is, $2\bar{\theta} = \theta_1 + \theta_2$.

The sandwich cylinder with pyramidal truss cores is designed on the basis of a simplified model of the shell-bar combined structure. The thicknesses of cylinder shells and core members are ignored. Fig. 2 shows the geometric model of a semi-unit cell in a ring plane.

The angle between the radial axes of the semi-unit cell is expressed as,

$$\varphi = \frac{\pi}{N_c}, \tag{1}$$

where N_c is the number of unit cells along the circumference. On the basis of the geometric relationships in Fig. 2, the angles between the core member and radial axis are given by

$$\tan \theta_1 = \frac{R_1 \sin \varphi}{(R_1 + t_c) - R_1 \cos \varphi}, \tag{2}$$

$$\tan \theta_2 = \frac{(R_1 + t_c) \sin \varphi}{(R_1 + t_c) \cos \varphi - R_1}, \tag{3}$$

Fig. 2. Relations between the amount of unit cell N_c and equivalent angle $\bar{\theta}$. For the structure fabricated in this work, the equivalent angle is 44.36° with N_c equaling to 12.

On the basis of the tangent function transformation,

$$\tan(2\bar{\theta}) = \tan(\theta_1 + \theta_2) = \frac{\tan \theta_1 + \tan \theta_2}{1 - \tan \theta_1 \tan \theta_2}, \tag{4}$$

By combining Eqs. (2) and (3), the equivalent angle $\bar{\theta}$ is obtained as follows:

$$\bar{\theta} = \frac{1}{2} \arctan \left[\frac{\left(2 + \frac{t_c}{R_1}\right) \frac{t_c}{R_1} \sin \frac{\pi}{N_c}}{\left(2 + \frac{2t_c}{R_1} + \frac{t_c}{R_1} \cdot \frac{t_c}{R_1}\right) \cos \frac{\pi}{N_c} - 2\left(1 + \frac{t_c}{R_1}\right)} \right], \quad \bar{\theta} \in (0°, 90°). \tag{5}$$

Therefore, $\bar{\theta}$ is a function of two dimensionless parameters, namely, t_c/R_1 and N_c.

$$\bar{\theta} = f\left(\frac{t_c}{R_1}, N_c\right). \tag{6}$$

For the structure in this work, N_c is set to 12 and the corresponding value of equivalent angle $\bar{\theta}$ is 44.36°, to ensure the pyramidal configuration, as shown in Fig. 2. However, the value of the equivalent angle $\bar{\theta}$ may change slightly in practice due to the joints at the nodes. Fig. 3 shows the geometric parameters that define a unit cell of the pyramidal truss cores.

The relative density $\bar{\rho}$ of the unit cell is given by

$$\bar{\rho} = \frac{4(l_1 + l_2)t^2}{(\pi/N_c)(R_2^2 - R_1^2)l_c} + \frac{6(2b - t)tc_0}{(\pi/N_c)(R_2^2 - R_1^2)l_c}, \tag{7}$$
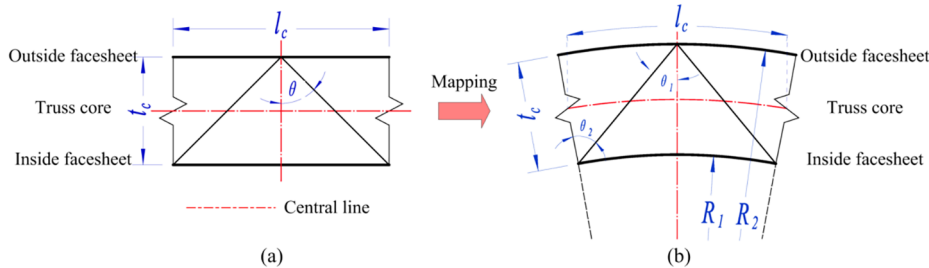

Fig. 1. Mapping process of pyramidal lattice truss in circumference: from (a) a rectangular unit cell in panel structure to (b) an annulus cell in cylinder structure.
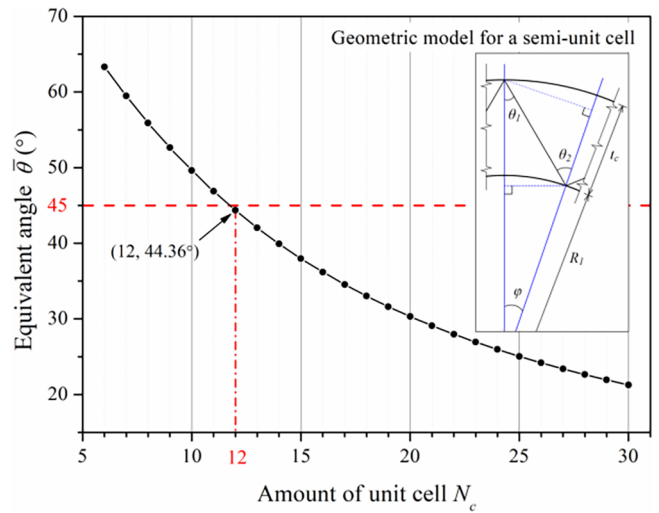
(a) Circumferential truss

(b) Longitudinal truss
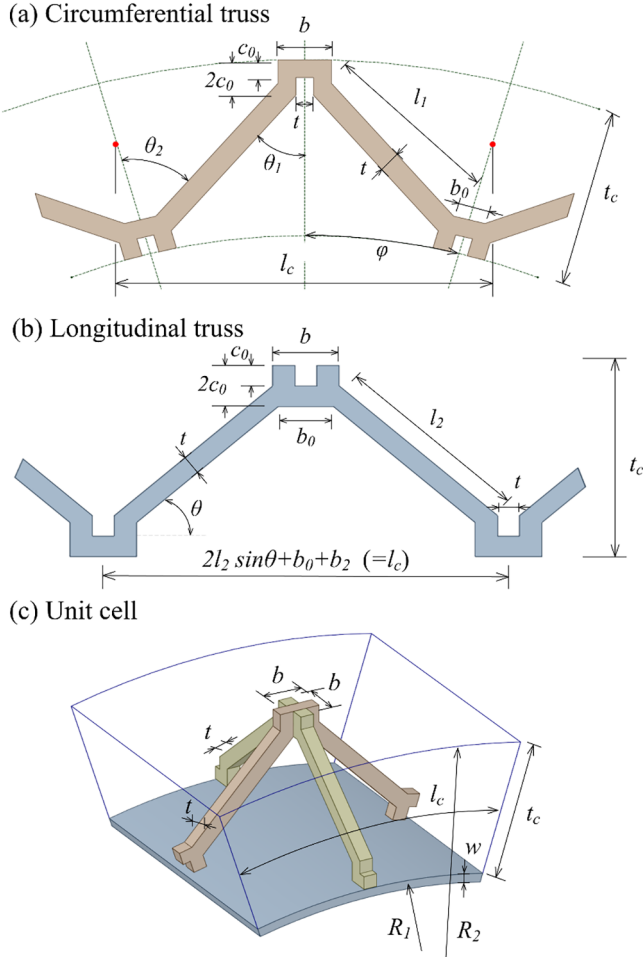

(c) Unit cell

Fig. 3. Geometries with relevant design variables of (a) circumferential truss, (b) longitudinal truss and (c) unit cell of snap-fitted pyramidal truss cores.

where t is the thickness of the core member, b is the width of the joints at the nodes, and l_1 and l_2 are the lengths of the core members. The two terms in Eq. (7) are the truss and nodal mass contributions, respectively. For a single layer pyramidal lattice truss, two independent stiffness constants, namely, out-of-plane compression E_c and shear stiffness G_c of the truss cores, are important for the mechanical performance. The analytical expressions are given as [28] +

$$E_c = E_s \cdot \sin^4 \theta \cdot \bar{\rho},$$ (8)

$$G_c = \frac{1}{8} E_s \cdot \sin^2 2\theta \cdot \bar{\rho},$$ (9)

where E_s is Young's modulus of the base material. The tensile and compressive stress–strain responses and modified Ramberg-Osgood fitting parameters of the base material in the present work are summarized in Appendix A.

2.2. Fabrication process

As shown in Fig. 4, the all-metallic sandwich cylinder with pyramidal truss core was fabricated through a four-step process: laser beam cutting (LBC), snap-fit assembly, vacuum brazing of the inner facesheet with truss cores and vacuum brazing of the outer facesheet with truss

cores. The truss row patterns with a thickness $t = 1.40$ mm, including circular and straight trusses, were cut by LBC from flat 304 stainless steel sheets. The maximum joint gap of the slots at the truss nodes was 80 μm. Coaxial circular trusses were aligned on a supporting base and the adjacent trusses were in a rotation angle of 15°. Straight trusses were then attached to circular trusses at the orthogonal direction through the snap-fit method, as shown in Fig. 4(b).

The inner facesheet was inserted into the snap-fit truss as a whole (Fig. 4(c)). Subsequently, the snap-fit truss and inner facesheet were bonded using a vacuum brazing approach. The Ni-7Gr-4.5Si-3.1B-3Fe braze alloy (Nicrobraze 31) was applied to the nodal regions of the assembled structure. The assembled lattice structures were placed in a high-temperature vacuum brazing furnace and heated at 10 °C/min to 600 °C (held for 10 min) and then to 900 °C at 10 °C/min (held for 20 min) to heat the assembly uniformly. Then, the assembly was heated at 10 °C/min to 1100 °C, for 10 min at a chamber pressure of 2×10^{-2} Pa. Subsequently, the furnace was naturally cooled to room temperature. Finally, as shown in Fig. 4(d), the three equal parts of the outer facesheet were bonded with the integrated lattice truss and inner facesheet by second vacuum brazing, which has the same process as the abovementioned process mentioned above. Table 1 summarizes the geometric parameters of sandwich cylinders with pyramidal truss core, with a resulting predicted relative density of 2.56%.

3. Experimental study

Fig. 5 shows the experimental setup. Static uniaxial compressive tests were performed on the sandwich cylinder in a 200 kN capacity electronic universal testing machine (CMT5205). The loading rate of the compression crosshead was 0.5 mm/min. A pair of stainless-steel disks with annular grooves was placed at the top and bottom of the sandwich cylinder to achieve a clamped boundary condition. The projection on each disk was in contact with the locating slot in the loading block to maintain the axially compressive conditions. Fast-curing resin was poured into the grooves to avoid local failures at the contact region.

A 3D digital image correlation (3D-DIC) system with two charge-coupled device (CCD) cameras was utilized to obtain the real-time deformation of the sandwich cylinder during compression. The image resolution of the two cameras was 1600×1200 pixels, and the sampling frequency was 1 fps. The 3D-DIC system was synchronically triggered by the CMT5205 to provide a unified starting time. Fig. 5(a) presents the speckle pattern on the outside cylinder surface.

Fig. 6 shows the compression load versus the displacement. All parts of the assembly in Fig. 5(b) were in close contact when the sandwich cylinder was pre-loaded to approximately 0.5 kN (point A in Fig. 6). The critical load was approximately 163.23 kN at point B. The sudden drop in load after the peak point and visual inspection of the specimen confirmed that the outer cylindrical surface failed with the local buckling near the top end. Non-symmetrical local buckling occurred near the loading end due to the defects produced during fabrication.

Fig. 7 shows the history of the full-field Mises strain calculated by the 3D-DIC system. Mises strain is defined as,

$$\bar{\varepsilon} = \frac{1}{\sqrt{2}} \sqrt{(\varepsilon_x - \varepsilon_y)^2 + (\varepsilon_y - \varepsilon_z)^2 + (\varepsilon_z - \varepsilon_x)^2 + 6(\varepsilon_{xy}^2 + \varepsilon_{yz}^2 + \varepsilon_{zx}^2)}$$ (10)

where ε_x, ε_y, and ε_z are the normal strain components and ε_{xy}, ε_{yz} and ε_{zx} are shear strain components. The strain components are calculated by definition from the exact space coordinate which is measured by the DIC system. The sandwich cylinder after the pre-loading stage is set as the base state in the analysis and the time zero point for DIC analysis. The computational domain is selected as the blue rectangular region in Fig. 7(a). Fig. 7(b–f) show the full-field Mises strain distribution and
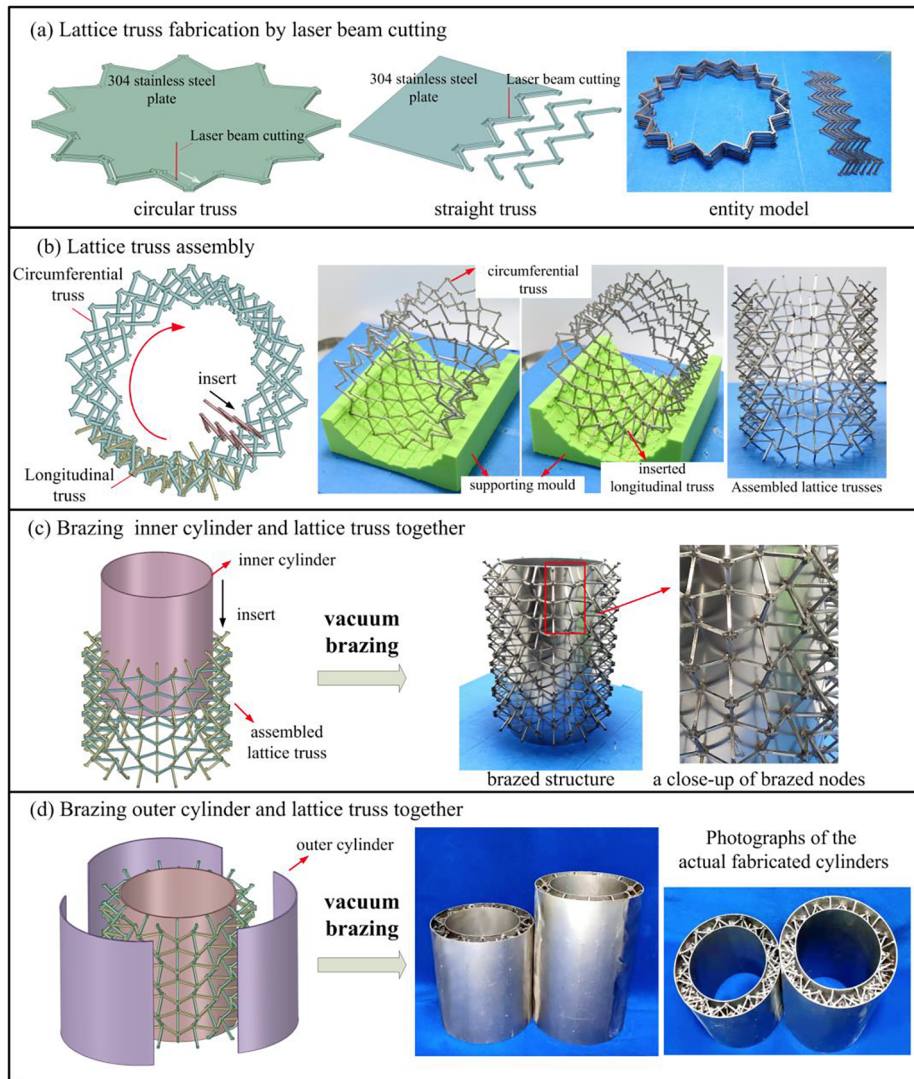
Fig. 4. Schematic of the fabrication and assembly method for manufacturing the sandwich cylinder with pyramidal truss cores.

Table 1
Design parameters for the sandwich cylinder with pyramidal truss cores (unit: mm).

l_1	l_2	t_c	c_0	b	b_0	t	φ	H	R_1	R_2	w
14.5	14.85	15	1.5	4.0	2.7	1.4	15°	160	45	60	1

buckling history of the sandwich cylinder. Local bucking occurs when the Mises strain value is 2.4% in the upper left of the rectangular computational domain (Fig. 7(e)). The outer facesheet in the failure zone is in plastic state at this time. Fig. 8 shows the quantitative buckling deformation in the z-direction of the sandwich cylinder measured by the 3D-DIC system. The local buckling behavior occurred between the adjacent nodes of the attachment. Furthermore, the buckling direction was 45° along the local truss direction, because the pyramid lattice configuration was orthotropic and weak 45° along the orthogonal truss.

Fig. 9 shows the Mises strains of seven pairs of marker points (A–G) selected in the undeformed reference image in Fig. 7(b). The Mises strains of the points in the buckling domain (points A, D, and E) increased dramatically when the critical load arrived and exceeded the yielding strain. The curve trend proves that the buckling course of the sandwich cylinder is nonlinear. Plastic deformation occurred in that area. Subsequently, local buckling failure occurred along the circumferential direction at B and C due to the initial defects.

The eigenvalue buckling and geometrical nonlinear stability of the fabricated sandwich cylinder are investigated using finite element method (FEM) analysis, as shown in Fig. 10. The model of the sandwich cylinder with pyramidal truss cores is based on the geometry of the test specimen in Table 1. Four-node doubly curved shell and two-node linear beam elements are used to construct the model. The total number of elements in the model is 13,544. All loading end nodes at the top surface are coupled with a central reference point with a linked rigid body, thereby enforcing a uniform displacement condition in the negative z-direction. The clamped boundary condition is set at the bottom surface. The failure mode of eigenvalue buckling is local buckling, which agrees well with experimental results in Fig. 7. The overestimation in eigenvalue buckling analysis is due to the initial imperfection of the fabricated cylinder. The collapse load of the imperfect
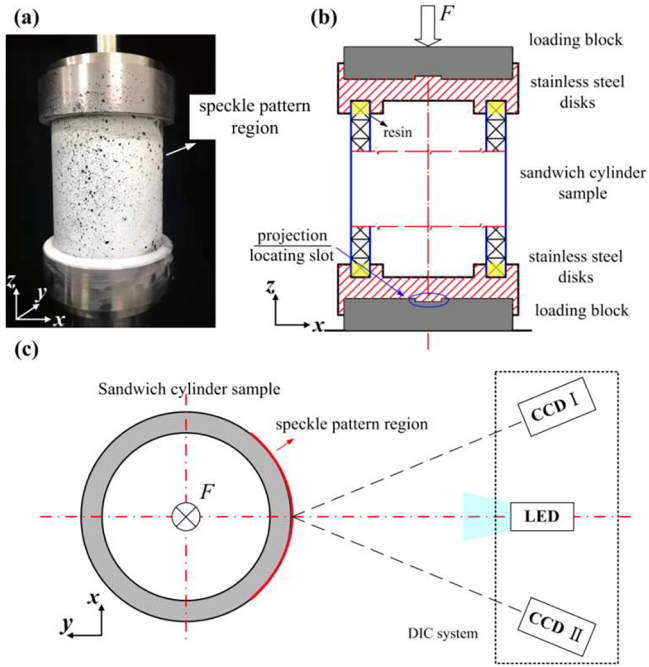
Fig. 5. Experimental setup of the sandwich cylinder under axial compression. (a) Photograph of the sample with speckle pattern before compression experiment, (b) schematic of the cross-section of the sandwich cylinder, (c) schematic of the DIC system.
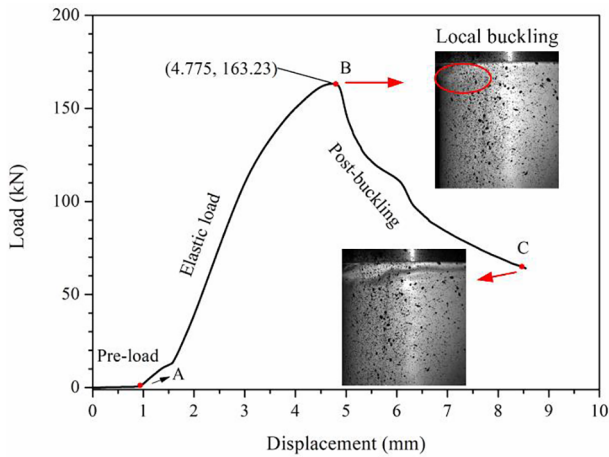

Fig. 6. Force–displacement curve of the sandwich cylinder under axial compression.

sandwich cylinder is calculated by the eigenmode-shape imperfection approach. The first order eigenmode shape obtained by linear buckling analysis in Fig. 10(a) is selected as the representative eigenmode shape and introduced into the perfect model. The imperfection amplitude ratio is based on the ratio of measured roundness error to the outside diameter of the sandwich cylinder. The roundness error is defined as the difference of the maximum and minimum outside diameters for the fabricated specimen. The imperfection amplitude ratio is set as 0.013 in the simulation. The bucking critical load of nonlinear buckling analysis is 146.12 kN, approximately 10.4% lower than the experimental value and the region near the top end experiences face yielding. In the actual experimental situation, unlike the numerical model, the tested cylinder

experiences local face yielding at the imperfection location and induces local buckling.

4. Failure maps under axial compression

In this section, the structural response of the sandwich cylinder with pyramidal truss core under clamped conditions subjected to compressive load P is studied theoretically. The truss core and facesheets are all made of stainless steel. As shown in Fig. 11, five failure modes are suggested: (1) Euler buckling of the sandwich cylinder (2) global buckling of the cylinder shell, (3) local buckling of the facesheet between reinforcements, (4) face yielding, and (5) core member buckling.

4.1. Euler buckling

For a long slender structure, the buckling mode of the sandwich cylinder is Euler buckling. On the basis of classical elastic stability theory [29], the Euler buckling load is as follows:

$$P_{EB} = \frac{k^2 \pi^2 (EI)_{eq}}{H^2}, \tag{11}$$

where $k = 2$ for a column with clamped-clamped ends, and $(EI)_{eq}$ is the equivalent flexural rigidity, which is $\frac{1}{4}\pi[(R_2 + w)^4 - (R_2 - t_c - w)^4]\left(\frac{2w}{t_c + 2w}E_s\right)$. The effects of core shear are ignored in this failure mode.

4.2. Global buckling

The buckling of the monolayer cylinder shell occurs when the connection between the cylinder sheet and lattice nodes is weak. On the basis of Stein's nonlinear pre-buckling deformation theory, the buckling load per unit area can be written as:

$$\sigma_{cr1} = \frac{c_1 E_s w}{R_2 \sqrt{3(1 - \nu^2)}} \tag{12}$$

where ν is Poisson's ratio and assumed as 0.3 for the current material. The buckling of the outer cylinder shell occurs before that of the inner shell due to its large radius. c_1 is the coefficient for the boundary conditions and the configuration. Parameter c_1 is different because of the configuration of the core area. For the isogrid configuration suggested by NASA, the parameter is often set as 3.47 [21]; for honeycombs, the values are from 2.25 to 9 and for the Kagome configuration, the value is set as 10.2 [30]. In the succeeding discussions, c_1 is set as 1.85, as suggested by the numerical simulations and the experimental results of the double shell with different geometric parameters λ summarized in [31].

$$\lambda = [12(1 - \nu^2)]^{1/4}\{R_1/[(R_2 w)^{1/2}]\}. \tag{13}$$

On the basis of the strain coordination condition and equivalence of the core area, the resultant critical load is given by

$$\begin{aligned} P_{GB} &= \sigma_{cr1} \cdot \left[2\pi(R_1 + R_2)w + \pi(R_2^2 - R_1^2)\frac{E_c}{E_s} \right] \\ &= 1.21\pi \frac{c_1 E_s w}{R_2}(2R_2 - t_c)\left(w + \frac{E_c}{2E_s}t_c\right). \end{aligned} \tag{14}$$

4.3. Local buckling

The facesheet between the nodal reinforcements forming a square area is subject to local buckling under axial compressive loads, and the
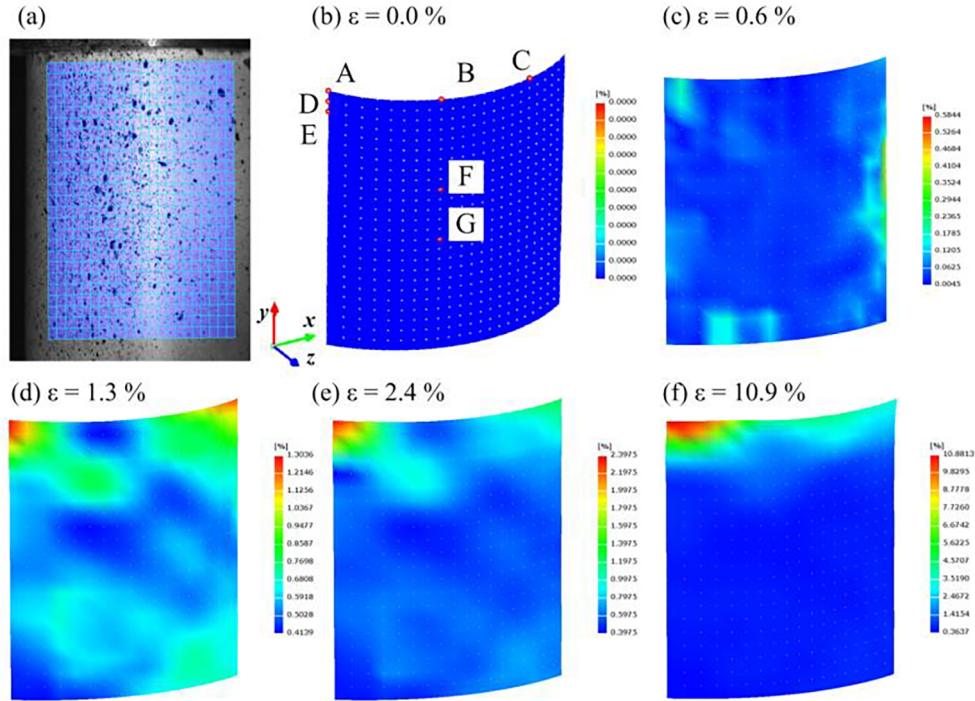
Fig. 7. Full-field Mises strain distribution of the sandwich cylinder, (a) computational domain, (b) maximum Mises strain $\varepsilon = 0.0\%$, (c) $\varepsilon = 0.6\%$, (d) $\varepsilon = 1.3\%$, (e) $\varepsilon = 2.4\%$, (f) $\varepsilon = 10.9\%$.

connection between the cylinder sheet and lattice nodes are strong. The local rectangular facesheet between nodal reinforcements experiences buckling with the enclosing four edges providing simply supported conditions, as shown in Fig. 10(c). The buckling load per unit area can be written as

$$\sigma_{cr2} = \frac{1}{\sin\theta} \frac{k\pi^2 E_s w^2}{12(1-\nu^2)(2t_c/\sin\theta)^2},$$ (15)

where $k = 4$, because the local rectangular facesheet is square.

$$P_{LB} = \frac{\pi^3 E_s w^2 \sin\theta}{2.93 t_c^2}(2R_2 - t_c)\left(w + \frac{E_c}{2E_s}t_c\right).$$ (16)

4.4. Face yielding

When the facesheet is relatively thick, the cylindrical shell fails with face yielding. The constraint follows the expression of maximum stress:

$$\sigma_{cr4} = \sigma_y^f,$$ (17)

where σ_y^f is the yield strength of the facesheet material. The critical load, P_{FY}, constrained by the yield strength is given by

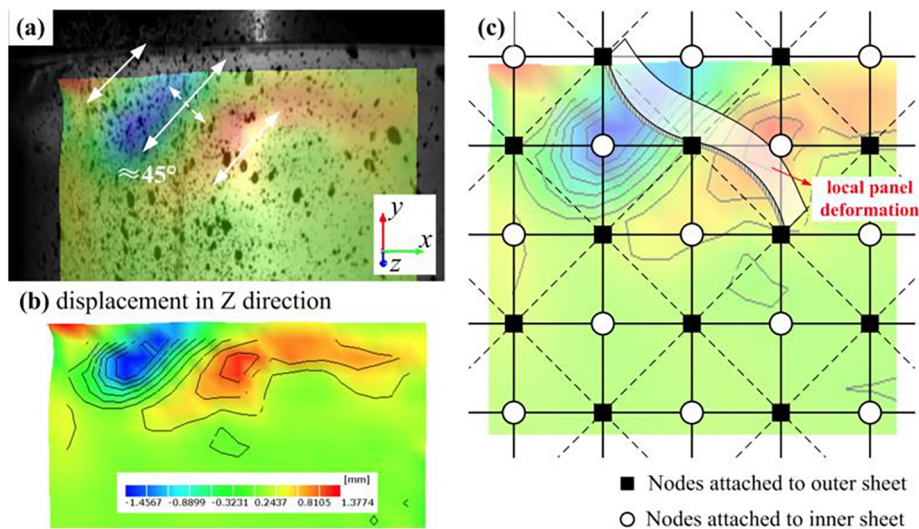$$P_{FY} = 2\pi\sigma_y^f(2R_2 - t_c)\left(w + \frac{E_c}{2E_s}t_c\right).$$ (18)

Fig. 8. Local buckling mode is influenced by truss orientation (a) surface speckle image of the local buckling failure region near the top end, (b) full-field displacement in the z-direction of the local buckling failure region, (c) node lines of the local buckling for the sandwich cylinder and failure direction.
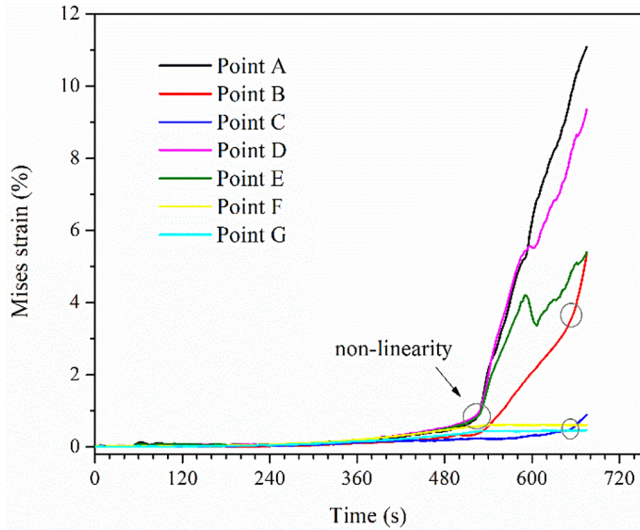
Fig. 9. Full-field Mises strain history of seven pairs of marker points in Fig. 7(b).
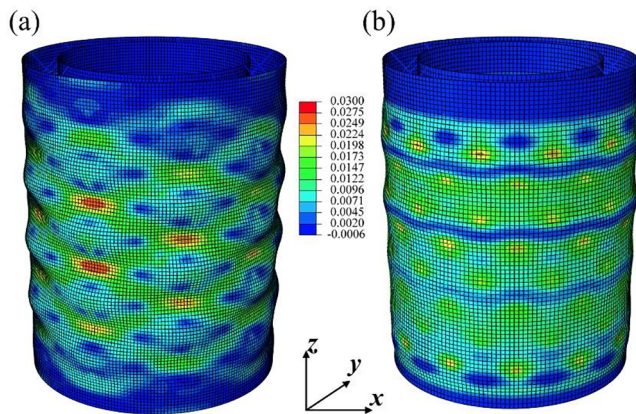

Fig. 10. FEM buckling failure analysis for the fabricated cylinder. (a) Eigenvalue buckling, (b) nonlinear stability analysis introducing initial defects.

4.5. Core member buckling

To obtain the critical load, truss joints are idealized as pin joints offering no rotational resistance between the core member and face-sheet [32,33]. The constraint for a single core member buckling is as follows:

$$P_{\text{single}} = \frac{k^2 \pi^2 E_s t^4 \sin^2 \theta}{12 t_c^2}, \tag{19}$$

where $k = 2$, because the pyramidal truss structure is considered to be stretching-dominated [15].

The contribution of the axial force component along the perpendicular direction of the truss is ignored. Thus, the uniaxial critical load on the entire truss core members is as follows:

$$P_{\text{core}} = \frac{2N_c}{\sin \theta} P_{\text{single}}. \tag{20}$$

On the basis of the strain coordination condition, the resultant critical load, P_{CB}, is given by:

$$P_{CB} = \frac{\pi(2R_2 - t_c)t_c E_c + 2\pi(2R_2 - t_c)wE_s}{\pi(2R_2 - t_c)t_c E_c} P_{core}$$

$$= \frac{t_c E_c + 2wE_s}{t_c E_c} P_{core}. \tag{21}$$

The prediction of failure modes and corresponding critical loads is verified by FEM methods with typical geometries under axial compression loads in the z-direction with fixed supports, summarized in Table 2. For the analysis of the sandwich cylinder shell and pyramidal truss core, the models of four-node doubly curved shell and two-node linear beam elements are presented, with mesh sizes of 4 mm and 2 mm, respectively. The shell and beam elements are tied together at truss joints. The effect of the initial imperfections is ignored. The theoretical results underestimate the critical loads compared with the FEM results.

4.6. Failure maps

The competing failure modes analyzed previously can be illustrated in failure mechanism maps. These failure maps are developed as functions of the nondimensional geometrical parameters normalized by the radius R_2, including t_c/R_2, w/R_2, H/R_2, and t/R_2. The boundaries of each failure mode are obtained by evaluating the lowest critical load with the change of two geometrical parameters, whereas the others are held constant. Not all of the five failure modes can occur, with the given geometrical constraints of two fixed parameters.

Fig. 12 shows the failure maps of the relationship between dimensionless variables, namely, the thickness of the cylinder shell w/R_2 and the core thickness t_c/R_2. The nondimensional width of the truss section t/R_2 and the nondimensional height of cylinder structure H/R_2 are set to 0.023 and 2.7, respectively. For the given normalized height H/R_2 of 2.7, the cylinder does not satisfy the assumption of a long slender structure; therefore Euler buckling will not occur. Face yielding occurs at the region where the thickness of the cylinder shell is sufficiently thin, because the structure is weak. With the increasing shell
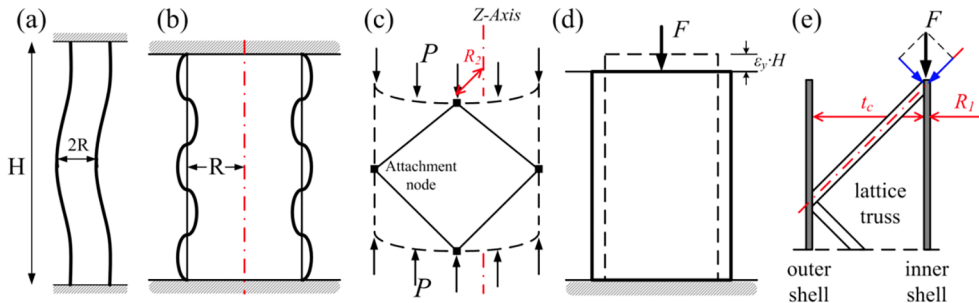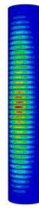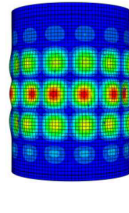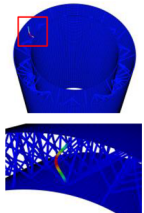

Fig. 11. Failure modes of the sandwich cylinder. (a) Euler buckling, (b) global buckling of cylinder shell, (c) local buckling between reinforcements, (d) face yielding, (e) core member buckling.

Table 2
Comparison of theoretical and FEM results on failure modes and corresponding critical loads with typical geometries.

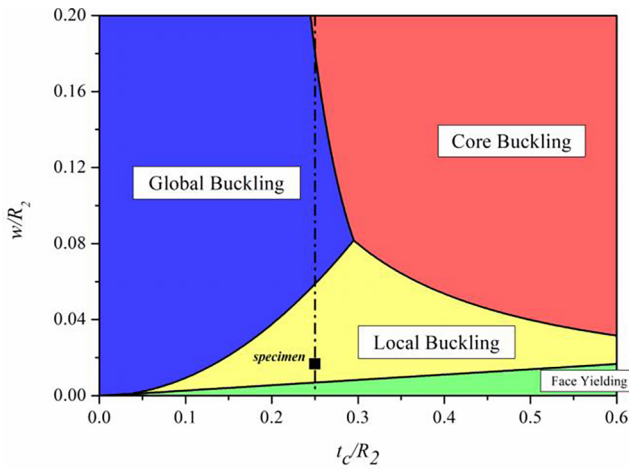| Failure modes	Euler buckling	Global buckling	Local buckling	Core member buckling
Nondimensional geometries $(t_c/R_2, w/R_2, H/R_2, t/R_2, N_c)$	$(\frac{1}{4},\frac{1}{50},120,\frac{3}{200},15)$	$(\frac{1}{10},\frac{2}{25},10,\frac{3}{200},30)$	$(\frac{1}{4},\frac{1}{60},2.5,\frac{1}{40},12)$	$(\frac{1}{2},\frac{2}{25},5,\frac{3}{200},15)$
Predicted failure loads (N)	2.24×10^5	1.79×10^8	1.086×10^6	3.392×10^6
FEM failure loads (N)	2.29×10^5	1.84×10^8	1.398×10^6	3.396×10^6
FEM Buckling modes				

Fig. 12. Failure mechanism map between the thickness of the cylinder shell w/R_2 and the core thickness t_c/R_2 ($t/R_2 = 0.023$).
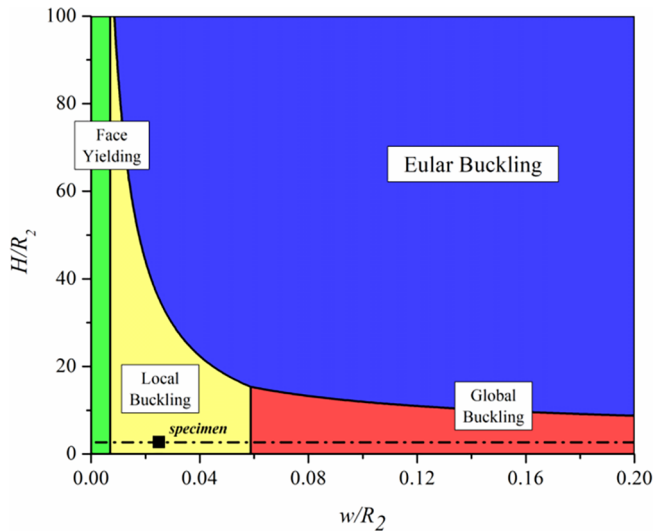

Fig. 13. Failure mechanism map between the height of the cylinder structure H/R_2 and the thickness of cylinder shell w/R_2 ($t/R_2 = 0.023$, $t_c/R_2 = 0.25$).

thickness and insufficient core thickness, global buckling occurs first, as shown in the upper left area in Fig. 12. When the core becomes sufficiently thick, the core area is the fragile region of the structure and core member buckling preferentially occurs, as shown in the upper right area in Fig. 12.

Fig. 13 shows the failure maps of the relationship between dimensionless variables, namely, the height of the cylinder structure H/R_2 and the thickness of cylinder shell w/R_2. Nondimensional parameters t/R_2 and t_c/R_2 are set to fixed values of 0.023 and 0.25, respectively. For the given nondimensional parameters of lattice truss member t/R_2 and t_c/R_2, core buckling hardly occurs. When the height of the cylinder structure becomes sufficiently large, the failure mode of the cylinder structure is Euler buckling, as shown in the upper right area in Fig. 13. For the structure that does not satisfy the slender rod assumption, the structure experiences face yielding, global buckling and local buckling in sequence with the increasing shell thickness. The black dot-dash line in Fig. 13, which represents the structure with three fixed values of t/R_2, t_c/R_2, and H/R_2, reveals this rule with changing w/R_2. The line in Fig. 13 also confirms this result.

5. Conclusions

In this work, a metallic sandwich cylinder with pyramidal truss cores was manufactured via geometric mapping and snap-fit method, thereby achieving compatibility of the cylinder shell and core members and reducing the weight of the core region. In comparison with the previously proposed lattice core configuration, the truss core of the structure in this work is fully pyramidal with a low relative density. Moreover, the open-cell topology of the core extends the usage of the sandwich panels to multi-functional applications. The failure maps of the sandwich cylinder are derived, including five competing failure modes, namely, Euler buckling, global buckling, local buckling, core buckling, and face yielding. The predicted results from the failure maps with variable dimensionless geometrical parameters match the experimental results. An axial compressive experiment using the DIC system revealed that local buckling pattern of the facesheet is influenced by the truss orientation. The proposed fabrication method can be extended to composite or other hybrid structures.

Conflict of interest

There is no conflict of interest.

Acknowledgment

Appendix A. Modified Ramberg-Osgood fitting for the material undergoes the brazed thermal cyclic loading

The true tensile and compressive stress–strain curves for the 304 stainless steel that undergoes the same thermal cyclic loading in the brazed process are fitted using the modified Ramberg-Osgood model [34]. This modified model is given by

$$\varepsilon = \begin{cases} \frac{\sigma}{E_0} + 0.002\left(\frac{\sigma}{\sigma_{0.2}}\right)^n & for\ \sigma \leq \sigma_{0.2} \\ \frac{\sigma - \sigma_{0.2}}{E_{0.2}} + \left(\varepsilon_u - \varepsilon_{0.2} - \frac{\sigma_u - \sigma_{0.2}}{E_{0.2}}\right)\left(\frac{\sigma - \sigma_{0.2}}{\sigma_u - \sigma_{0.2}}\right)^m + \varepsilon_{0.2} & for\ \sigma > \sigma_{0.2} \end{cases}.$$

(A.1)

Table A.1 lists the parameters of the modified Ramberg-Osgood model shown in Fig. 14. Young's modulus Es and plastic yielding strength σ_y use the average value for the tensile and compressive stress–strain curves, namely, 174.2 MPa and 186.5 GPa, respectively.

Table A.1
Parameters of the modified Ramberg-Osgood fitting of the tensile and compressive response.

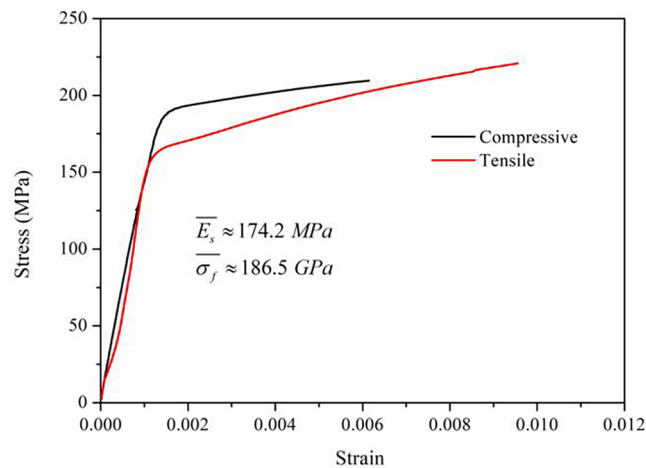| Model	$\sigma_{0.2}$ (MPa)	E_0 (GPa)	n	$\varepsilon_{0.2}$	ε_u	σ_u (MPa)	$E_{0.2}$ (GPa)	m
Compressive	199.3	167.5	18.88	0.0033	0.0062	209.58	4.30	2.49
Tensile	173.6	180.8	8.23	0.0032	0.0096	220.81	5.69	1.62

Fig. 14. Compressive and tensile stress–strain responses of the 304 stainless steel after exposure to the thermal cycle used for brazing.

References

[1] Wadley HNG. Multifunctional periodic cellular metals. Philos Trans 2006;364:31–68.
[2] Gibson LJ, Ashby MF. Cellular solids: structure and properties. Cambridge University Press; 1999.
[3] Hu Y, Li W, An X, Fan H. Fabrication and mechanical behaviors of corrugated lattice truss composite sandwich panels. Compos Sci Technol 2016;125:114–22.
[4] Valdevit L, Wei Z, Mercer C, Zok FW, Evans AG. Structural performance of near-optimal sandwich panels with corrugated cores. Int J Solids Struct 2006;43:4888–905.
[5] Cote F, Biagi R, Bart-Smith H, Deshpande VS. Structural response of pyramidal core sandwich columns. Int J Solids Struct 2007;44:3533–56.
[6] Queheillalt DT, Wadley HNG. Titanium alloy lattice truss structures. Mater Des 2009;30:1966–75.
[7] Zok FW, Waltner SA, Wei Z, Rathbun HJ, Mcmeeking RM, Evans AG. A protocol for characterizing the structural performance of metallic sandwich panels: application to pyramidal truss cores. Int J Solids Struct 2004;41:6249–71.
[8] Wang J, Evans AG, Dharmasena K, Wadley HNG. On the performance of truss panels with Kagomé cores. Int J Solids Struct 2003;40:6981–8.
[9] Sugimura Y. Mechanical response of single-layer tetrahedral trusses under shear loading. Mech Mater 2004;36:715–21.
[10] Zhang G, Li M, Bing W, Wu L. Mechanical behaviour of CFRP sandwich structures with tetrahedral lattice truss cores. Compos B 2012;43:471–6.
[11] Chiras S, Mumm DR, Evans AG, Wicks N, Hutchinson JW, Dharmasena K, et al. The structural performance of near-optimized truss core panels. Int J Solids Struct 2002;39:4093–115.
[12] Dong L, Deshpande V, Wadley H. Mechanical response of Ti–6Al–4V octet-truss lattice structures. Int J Solids Struct 2015;60–61:107–24.
[13] Feng LJ, Wu LZ, Yu GC. An Hourglass truss lattice structure and its mechanical performances. Mater Des 2016;99:581–91.
[14] Han D, Tsai SW. Interlocked composite grids design and manufacturing. J Compos Mater 2003;37:287–316.
[15] Deshpande VS, Ashby MF, Fleck NA. Foam topology: bending versus stretching dominated architectures. Acta Mater 2001;49:1035–40.
[16] Lu TJ, Valdevit L, Evans AG. Active cooling by metallic sandwich structures with periodic cores. Prog Mater Sci 2005;50:789–815.
[17] Wang JT, Yuan W, Liu YW, Song HW, Huang CG. High-power laser resistance of filled sandwich panel with truss cores: Ablation mechanisms and numerical simulation. Compos Struct 2018;203:574–84.
[18] Wu Y, Wang J, Song H, Ma T, Wu W, Li J, et al. High-power laser resistance of filled sandwich panel with truss core: an experimental study. Compos Struct 2018;193. S0263822317341958.
[19] Fan H, Fang D, Chen L, Dai Z, Yang W. Manufacturing and testing of a CFRC sandwich cylinder with Kagome cores. Compos Sci Technol 2009;69:2695–700.
[20] Huybrechts SM, Meink TE, Wegner PM, Ganley JM. Manufacturing theory for advanced grid stiffened structures. Compos A 2002;33:155–61.
[21] Meyer R, Harwood O, Harmon M, Orlando J. Isogrid design handbook. 1973.
[22] Shu J, Sun F, Fan H, Fang D. Fabrication and testing of composite orthogrid sandwich cylinder. Compos Sci Technol 2017;142:171–9.
[23] Hutchinson JW, He MY. Buckling of cylindrical sandwich shells with metal foam cores. Int J Solids Struct 2000;37:6777–94.
[24] Jian X, Ghosh R, Li M, Vaziri A, Wang Y, Wu L. Sandwich-walled cylindrical shells with lightweight metallic lattice truss cores and carbon fiber-reinforced composite face sheets. Compos A Appl Sci Manuf 2014;56:226–38.
[25] Xiong J, Ghosh R, Ma L, Ebrahimi H, Hamouda AMS, Vaziri A, et al. Bending behavior of lightweight sandwich-walled shells with pyramidal truss cores. Compos Struct 2014;116:793–804.
[26] Yang J, Jian X, Li M, Zhang G, Wang X, Wu L. Study on vibration damping of composite sandwich cylindrical shell with pyramidal truss-like cores. Compos Struct 2014;117:362–72.

[27] Agarwal BL, Sobel LH. Weight comparisons of optimized stiffened, unstiffened, and sandwich cylindrical shells. J Aircraft 1976;14:1000–8.

[28] Queheillalt DT, Murty Y, Wadley HN. Mechanical properties of an extruded pyramidal lattice truss sandwich structure. Scr Mater 2008;58:76–9.

[29] Timoshenko SP, Gere JM, Prager W. Theory of elastic stability, second edition. J Appl Mech 1962;29:220.

[30] Sun FF, Fan HL, Zhou CW, Fang DN. Equivalent analysis and failure prediction of quasi-isotropic composite sandwich cylinder with lattice core under uniaxial compression. Compos Struct 2013;101:180–90.

[31] Wang LRL. Discrepancy of experimental buckling pressures of spherical shells. AIAA J 1967;5. 357-&.

[32] Wicks N, Hutchinson JW. Optimal truss plates. Int J Solids Struct 2001;38:5165–83.

[33] Yuan W, Song H, Huang C. Failure maps and optimal design of metallic sandwich panels with truss cores subjected to thermal loading. Int J Mech Sci 2016;115–116:56–67.

[34] Rasmussen KJR. Full-range stress–strain curves for stainless steel alloys. J Constr Steel Res 2003;59:47–61.